Materials Research Express

PAPER • **OPEN ACCESS**

Electromechanical mode imaging of MoS_2 drum resonators

To cite this article: Julia García-Pérez *et al* 2025 *Mater. Res. Express* **12** 075002

Materials Research Express

PAPER

Electromechanical mode imaging of MoS_2 drum resonators

Julia García-Pérez, Daniel Granados and Ramón Bernardo-Gavito*

IMDEA Nanociencia. Faraday, 9, 28049 Madrid, Spain

* Author to whom any correspondence should be addressed.

E-mail: ramon.bernardo@imdea.org

Keywords: MEMS, two-dimensional materials, optomechanics, acoustics, resonators

Supplementary material for this article is available online

OPEN ACCESS

RECEIVED
5 May 2025

REVISED
23 June 2025

ACCEPTED FOR PUBLICATION
4 July 2025

PUBLISHED
16 July 2025

Abstract

Recent studies of optomechanical resonators based on 2D materials, are mainly focused on their response at a fixed point. Most studies focus on the oscillating behaviour of the centre of the system, where the amplitude of the fundamental mode is maximum. This methodology overlooks the spatial distribution of higher frequency oscillation modes in which the nodal lines cross the central point. These modes are of interest as they contain information of the stress and defect profiles, among other physical properties of the resonator/cavity system. Understanding the frequency response and spatial distribution of these modes is key both for fundamental science but also for the technological exploitation of these devices. In this work, we study the mechanical modes of few-layer MoS_2 electromechanical resonators down to 5 K with circular and rectangular boundary conditions. We have developed a novel technique to perform radio frequency spectral mapping of the resonators' optical response as they oscillate in real time. With this technique, we gain direct insight on the spatial distribution of the strain fields in the modal spectra of our devices.

Vibrations and waves are an inherent part of nature. From quantum systems [1] to gravitational waves [2], most scientific studies involve oscillations in one form or another. Large oscillations like those measured by earthquake early detection systems [3, 4], and molecular scale vibrations such as those used in infrared and Raman spectroscopy [5], are monitored every day for many different fields spanning from astrophysics to early disease diagnostics. Since the advent of two dimensional materials, the study of their mechanical vibrations and strain dependences has emerged as a fundamental research field with many open questions and interesting applications [6] in Nanoelectromechanical systems (NEMS). By their own nature, devices made of two dimensional materials are in the mesoscopic scale. Their ultra-thin nature gives rise to quantum phenomena, such as out-of-plane electronic confinement or quantized emission [7, 8]. However, their lateral dimensions are typically large enough that their mechanical properties can be effectively described within classical frameworks, in particular in the case of opto-mechanical oscillators [9].

In the nanoscale domain, NEMS are exploited for transducing electrical signals to mechanical motion, and vice-versa [10]. Mechanical drum resonators based on two-dimensional materials are a specific kind of NEMS that have become a hot research topic over the last few years [11–13]. From the fundamental point of view, they show a strong nonlinear response and can withstand large deformations without reaching rupture [14]. They are technologically significant because they exhibit Q-factors in the tens of thousands, and possible much higher, in the frequency range of tens of megahertz (MHz) to gigahertz [15–18] and exhibit electro-optical [9] and electro-acoustical [19] transduction. They embody an interesting playground for the fundamental study mechanical systems [20–22] and dynamical processes at surfaces [9]. When the thickness of the 2D material is sufficiently small to allow some transparency in the UV–vis-NIR, a short of Fabry–Perot etalon [15] can be manufactured in the form of a nanoelectromechanical-optical system (NEMOS). The performance of the drum-head as a membrane or a plate, strongly depends on the thickness of the material and the baseline strain profile [23]. These also influence the optical cavity in terms of resonance wavelengths and finesse. Built-in stress induced during the deterministic transfer of the 2D material onto the cavity resonator (see Methods), can lead to anisotropies in the

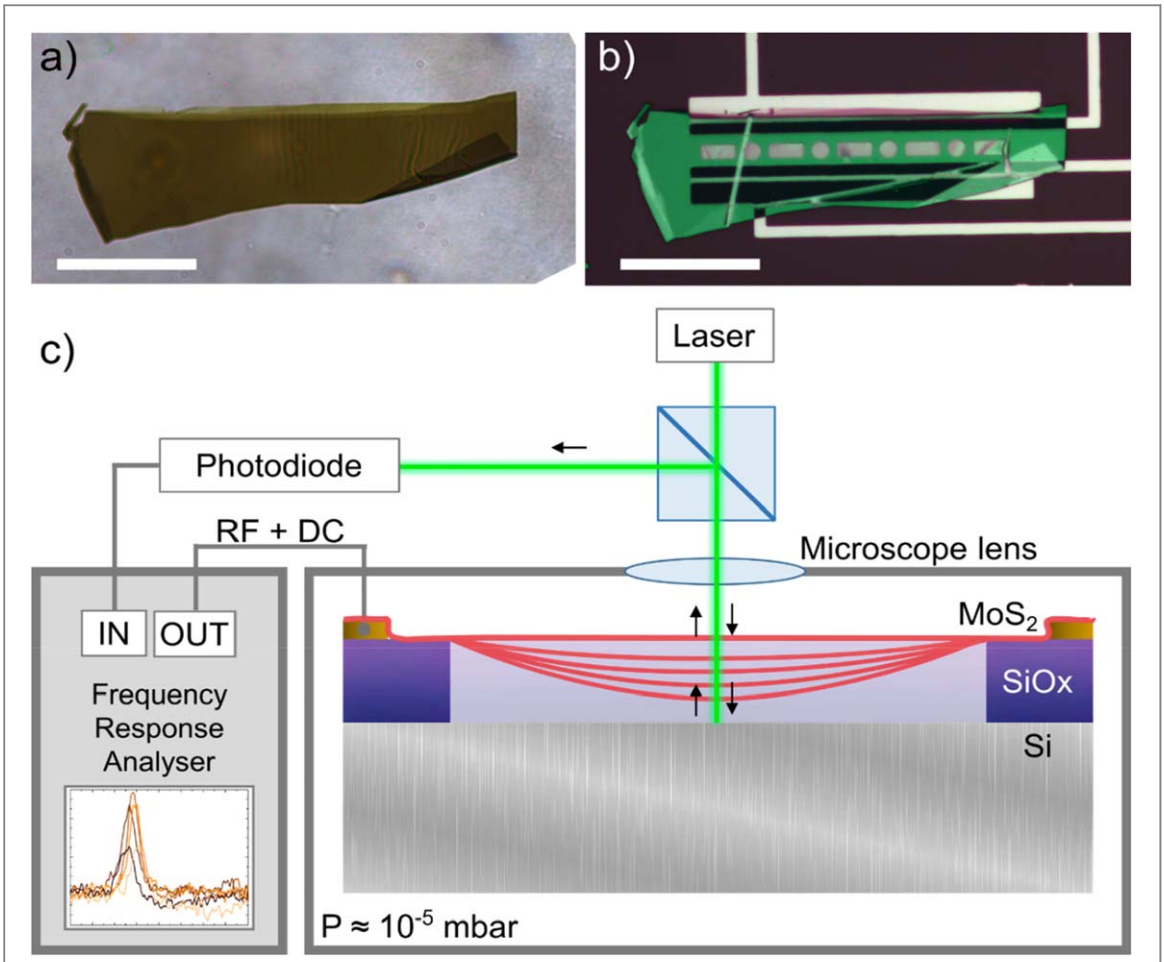

Figure 1. Deterministic transfer of MoS_2 and experimental set up. (a), Exfoliated MoS2 flake on a PDMS stamp. Scale bar 40 μm. (b), Optical image of the same flake after being deterministically transferred onto rectangular and circular wells with Ti/Au contacts. The colour of the flake is given by the refractive index and the strain contrast between the gold layer (supported-black), the SiO_x substrate (supported-green) and the Si substrate (suspended-light pink). Scale bar 40 μm. (c), Schematic representation of the system set-up for the electro-optical characterization of the MoS_2 drum resonators. RF sweeps are conducted while the reflected intensity as a function of frequency is recorded to acquire the spectral maps.

mode shapes [24]. Point defects or adsorbates on the MoS_2, can also impact the symmetries of the mechanical modes. In general, built-in stress and defects lift-up the degeneracy of many of the modes. There are multiple approaches for the study of 2D resonators [25]. In the last years, studies of the frequency dependence and spatial mapping of the vibrational modes of micrometre-scale resonators based on different 2D materials have been carried out in different micromechanical systems such as circular graphene drums [26], black phosphorus resonators [27], boron nitride [28] , graphene [29], or the anisotropic response study [30] of $CdNb_2O_6$ layered perovskites. Some works focus on single point measurements of the frequency spectra [31–33], estimating the modal response from them and thus overlooking the spatial distribution of the mechanical mode deformations i.e. and thus, of the strain fields. Other research show extended images of some of the resonant modes of drum resonators but as a collateral result from their main topics [24, 34, 35]. To enhance the capture efficiency in biomedicine mass spectroscopy, square membrane resonators are used to amplify the capture area and avoid degenerate mechanical modes [36, 37].

In this work, we performed a systematic study of the modal spectra of different MoS_2 resonators. We shape our drum resonators as a two-terminal capacitive structure utilising electrical actuation and optical readout [32]. Our resonators consist of MoS_2 flakes suspended over circular and rectangular holes. The pits are etched on a SiO_x/Si highly doped substrate by means of a lithography process (see methods). Figures 1(a)–(b) shows a crucial step of the microfabrication process of one of the devices, the exfoliation and transfer of the 2D material. The system behaves in a way where one of the electrodes is fixed, and the other is a movable plate or a membrane allowed to oscillate within a certain range and boundary conditions, in a similar fashion to an electrostatic speaker or a microphone. This allows for the electromechanical actuation or sensing, since an applied electric field will charge the capacitor and deform the 2D membrane towards the substrate, leading to a change in the inter-plate distance and thus the capacitance of the structure [38]. The experimental set up for frequency mapping of the resonators is shown in figure 1(c). A through-the-lens scheme is employed for optical

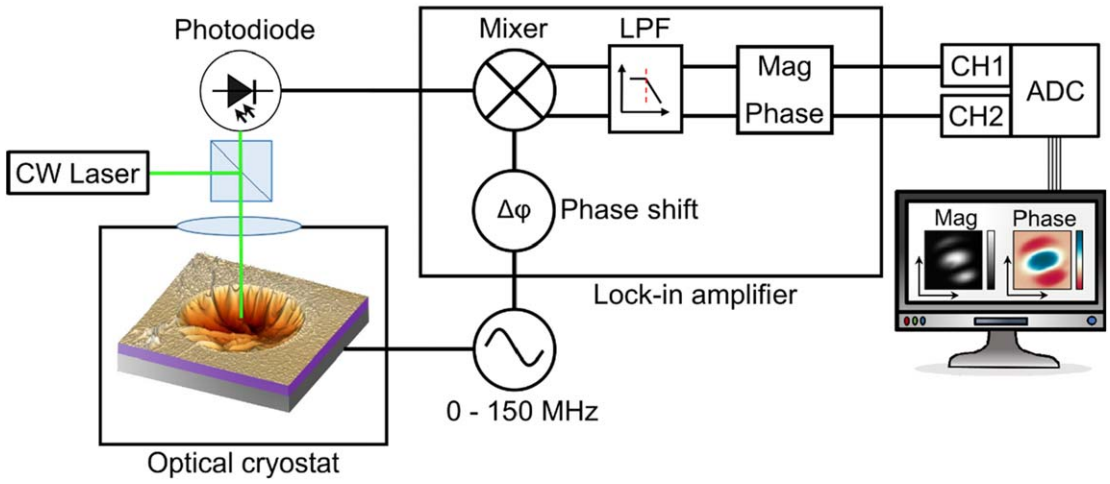

Figure 2. Experimental set up for high resolution mode imaging. Schematic diagram of the lock-in acquisition setup for imaging of the vibrational modes of the MoS_2 resonators.

illumination and read-out. A CW 532 nm laser is guided by a series of mirrors and beam-splitters to the microscope objective creating a diffraction limited spot onto the device under test. The reflected light is collected and routed into a fast photodiode for imaging and data acquisition. The electrical driving is achieved using an RF feedthrough installed in the vacuum chamber. RF sweeps are performed while the reflected optical intensity is recorded as a function of frequency to acquire the spectral maps.

The employed MoS_2 is semi-transparent, and under illumination with a diffraction limited spot, the system provides an optical contrast proportional to coupling between the 2D material thickness, its complex refractive index changes induced by mechanical motion, and the changes during the oscillation of the resonator geometry in vibrational modes. The quasi-Fabry–Perot cavity is formed by the MoS_2 acting as a top oscillating mirror and the Si substrate as fixed bottom mirror. This type of NEMOS have been designed to have characteristic optical lengths in the range of hundreds of nanometres, comparable to the wavelengths of visible radiation. Under mechanical motion of the top mirror, it provides interferometric contrast as the inter-plate distance changes [15]. This contrast is also affected by the dynamical evolution of the membrane, as the optical properties of the two-dimensional material (such as bandgap nature, refractive index or absorption coefficient) change when subjected to strain induced by mechanical deformation or oscillations [39].

In this article we identify and characterise the resonant modes of circular and rectangular 2D drum resonators to gain new insights into this type of NEMOS. This method combines optical microscopy and radio frequency response mapping of the devices under cryogenic and vacuum conditions. It utilises changes in the overall reflectivity of the optical cavity and high sensibility optical imaging of the modes using lock-in techniques. With this information we figure out the eccentricity of the circular device, the dynamic nature of the system (either membrane or plate) and the phase velocity of the mechanical wave.

MoS_2 circular resonators actuation and readout

Our devices consist of 45 nm-thick parallel Ti/Au electrodes defined by optical lithography and lift-off deposited on top of a SiO_2/Si substrate. Circular and rectangular wells are defined in a second lithography step followed by wet etching of the SiO_x. The MoS_2 flakes are deterministically transferred onto the well. Details on the fabrication process are further detailed in the Methods section and in Supplementary Information figures S1–S3. The devices are placed in a closed-cycle optical cryostat, equipped with XYZ positioners and an XYZ scanner which allow us to navigate and scan the resonators under a microscope objective with high spatial resolution (figure 2). A constant DC voltage can be used to set a pre-tension of the membrane while a waveform generator sends an RF signal to actuate the electromechanical resonator at the selected frequency range. The optical readout is performed in a through-the-lens approach, where a diffraction limited spot of a 532 nm CW laser, is focused on the surface of the MoS_2. The signal reflected by the Fabry–Perot etalon is send back into a high bandwidth (250 MHz) photodiode. The output signal of the photodiode is fed to the input ports of the scanner electronics, or to a digital signal processor acting as a frequency response analyser or lock-in amplifier, depending on the measurement scheme.

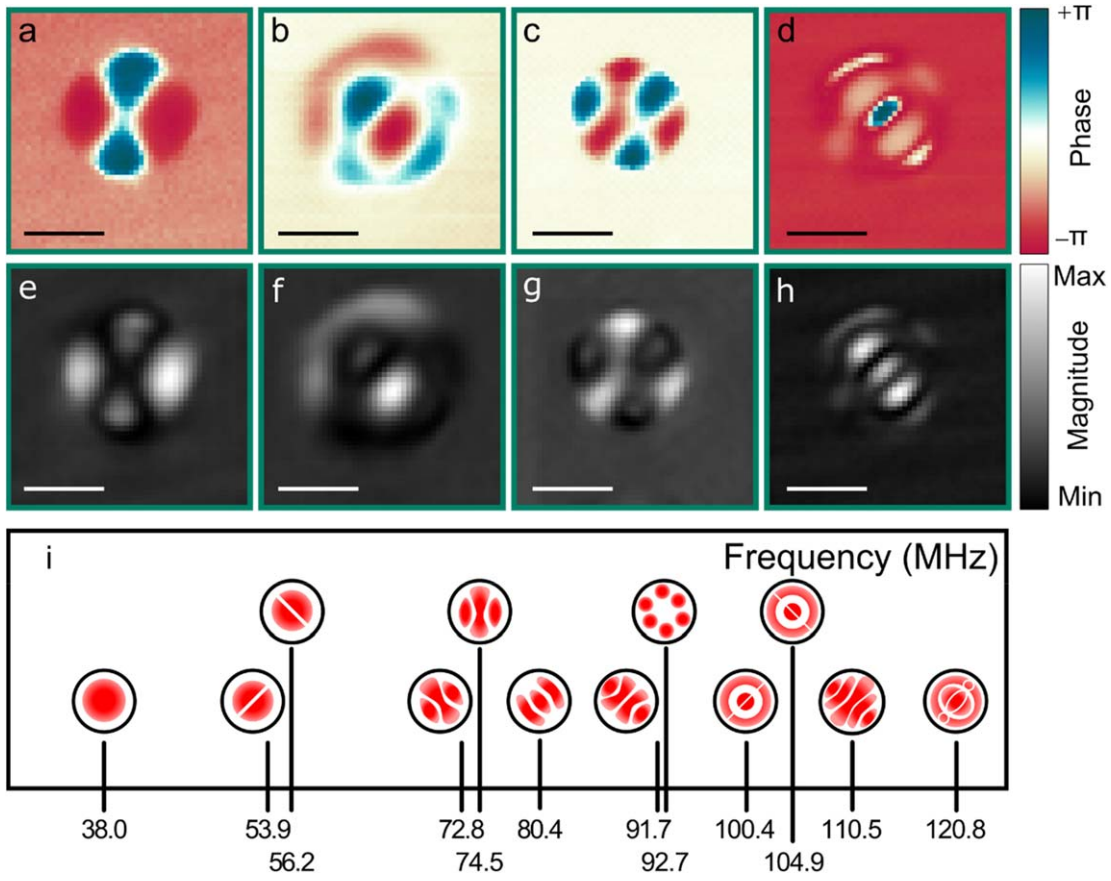

Figure 3. High resolution imaging of resonant modes at 5 K. (a)–(d), Phase images from experimental results (e)–(h) Magnitude images from experimental results. Scale bar 2.5 μm. (i), Frequency chart of the measured modes by this technique.

High resolution mode imaging

After the spatial modes and their frequencies have been identified by the frequency response maps (see supplementary S4), high sensitivity images can be obtained by switching the photodiode reflected intensity signal from the frequency response analyser to a lock-in amplifier. Lock-in filtering allow us to obtain high fidelity magnitude and phase images of very narrow frequency windows, muzzling spurious noise from the environment. To do so, we perform fast spatial scans at a very specific frequency and a fixed phase, to simultaneously record the magnitude and phase shift (or X and Y) outputs of the lock-in amplifier as raster images, just as other scanning probe techniques do [40].

A schematic representation of the high resolution imaging setup is shown in figure 2. For this step, we use an external waveform generator and DC power supply through a bias-tee to tune the actuation parameters in a broader voltage range from 1 mV to 20 V RMS. The filtered signals are fed to the analog-to-digital ports of the scanner electronics to obtain live raster images of the resonant modes.

Mode imaging of circular resonators

At room temperature, the frequency response of the device presents several overlapping peaks and a continuous response across most of the spectral range (Supplementary information figure S5). Spectral maps also reveal a spatial overlapping of the modes, which makes very difficult to assign a specific frequencies to individual modes (Supplementary video 1). Magnitude images show small amplitude variations and disordered mode shapes.

At lower temperatures, we would expect an enhancement in the quality factor [41] and an increase of the resonant frequencies (Supplementary video 2). This reduces the overlaps between modes, making them more distinguishable from each other. Figure 3 shows a series of magnitude and phase images taken at 5 K on a 25 nm-thick MoS_2 resonator showing different vibrational modes. At first sight, we can see that the modes do not correspond to a circular system, since all images do not show radial symmetry and present a preferential axis instead. Despite the circular boundary conditions of the well, the modes resemble the behaviour of an elliptical drum [42, 43]. This can be attributed to imperfections in the lithography process which can lead to distortions in

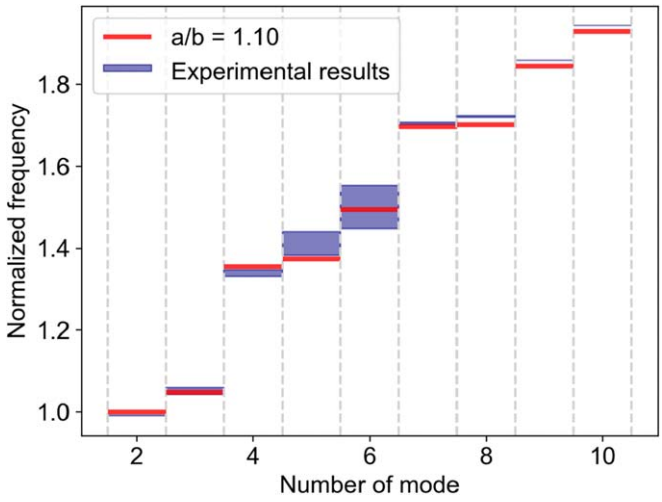

Figure 4. Finite element fitting with experimental results. Red lines point out the theoretical frequency of an elliptical membrane of 1.10 axis ratio, whereas the blue area select the response region of the resonator.

the actual shape of the etched holes, extended defects or thickness variations across the flake; but most likely from induced stress in a preferential direction coming from the deterministic mechanical exfoliation process. Another hypothesis regarding the atomic arrangement of the material has been presented in a detailed study focused on $CaNb_2O_6$ [30]. This material is already intrinsically anisotropic due to its highly asymmetric crystal structure in the a–b plane, so the presented modes are anisotropic. The time evolution of the mode can be reconstructed by concatenating a series of images of constant phase differences (Supplementary video 3).

In figure 4, all the observed modes at 5 K between 30 MHz and 130 MHz are presented in sequential order. Higher resolution images of the vibrational modes are presented in Supplementary figure S6.

At room temperature, mechanical resonances appear as broad, overlapping modes. Upon cooling, these modes progressively break their degeneracy, revealing distinct resonances characterized by a rotation of their primary axes with frequency. Additionally, the increase in quality factor at lower temperatures uncovers previously unresolved modes, enabling detailed analysis of mode shapes and spatial anisotropies. The measured resonance frequencies and spatial profiles of the modes are consistent with finite element numerical results in elliptic coordinates [43]. Following the frequency of the modes, we gather information of the axis ratio of the apparent ellipse. Through the theoretical study, we figure out that the aspect ratio of the system is $a/b \approx 1.10$, so the eccentricity is $e = 0.416$. As we show in figure 5, error bars mark the frequency range in which the mode exists due to nonlinear features.

Calculated phase velocity with rectangular modes

To understand more deeply our devices, and to avoid uncontrolled asymmetries in the shape of the device, we fabricate wells with rectangular boundary conditions and different aspect ratios. At the room temperature, we observe the expected behaviour, with clear degenerated modes (Supplementary information figure S7), small oscillation amplitudes and low quality factors. Otherwise, at 5 K we measure the represented modes in the chart in figure 5. All the located modes are presented in the Supplementary information (figure S8).

In figure 6, we distribute the measured modes by the number of antinodes in each axis. The modes shaded in grey in the chart represent those that could not be directly measured due to limitations arising from the nonlinear response observed at mode (3 ,1). Specifically, the amplitude of this mode is sufficiently large that it causes the system's frequency response to deviate from linearity, thus impacting the accessibility of measure (2,5) and (1,6) modes. This nonlinearity introduces significant challenges when attempting to characterize the behaviour of the system. As the amplitude increase, the jump-down frequency becomes higher, so the device response spans around 4 MHz at 2 Vpp.

When plotting the mode number against the measured frequency, we observe that the trend of the resulting curve indicates the system behaves as a membrane rather than a plate, aligning with the behaviour predicted by equation (1) [44]. Each eigenfrequency determines a different out-of-plane vibration that can be expressed as a function of two natural numbers (m,n), which are the quantity of antinodes in each axis onto the mode of vibration.

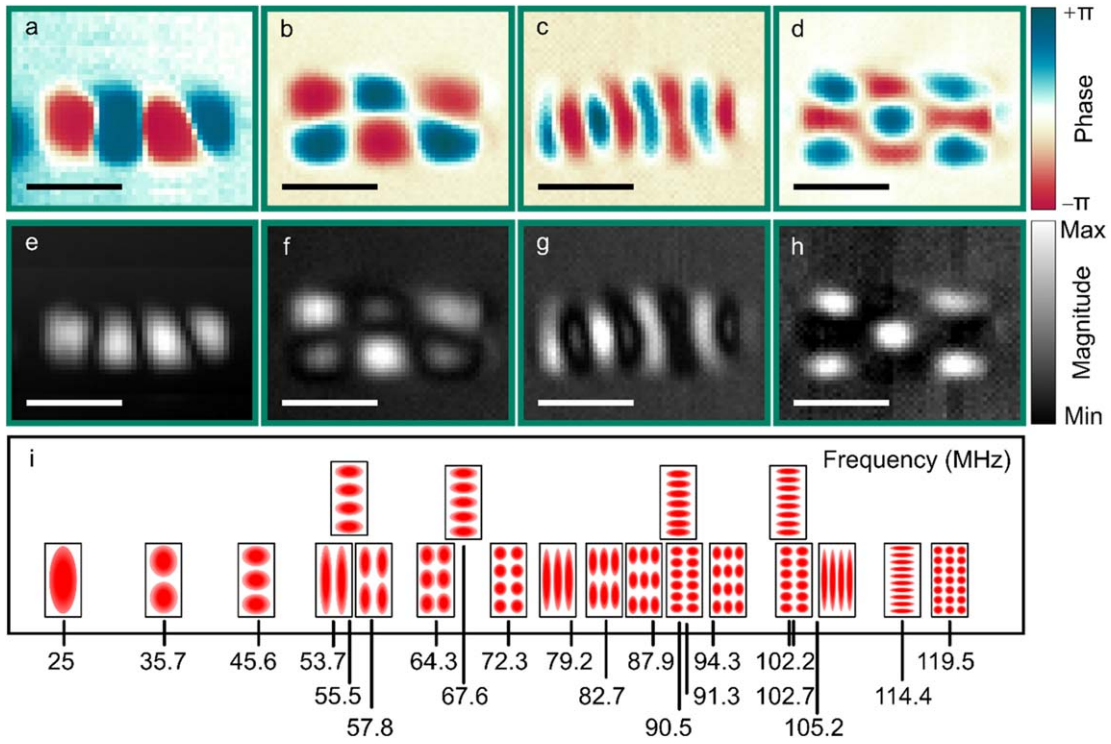

Figure 5. High resolution imaging of rectangular resonant modes at 5 K. (a)–(d), Phase images from experimental results. (e)–(h) Magnitude images from experimental results. Scale bar 5 μm (i), Frequency chart of the measured modes.

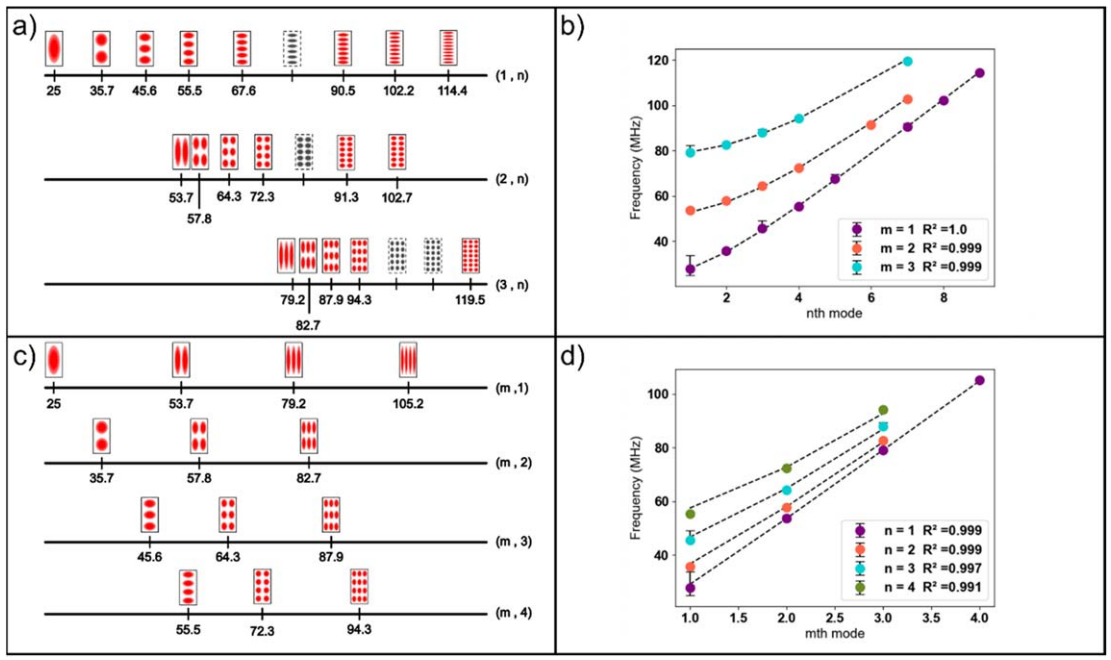

Figure 6. Chart of measured rectangular modes at 5 K. (a) Fixed number of antinodes in the horizontal axis. (b) Fitting of these modes using the membrane theoretical behaviour. (c) Fixed number of antinodes in the vertical axis. (d) Fitting of these modes using the membrane theoretical behaviour.

$$f_{m,n} = \frac{c}{2}\sqrt{\left(\frac{m}{L}\right)^2 + \left(\frac{n}{H}\right)^2} \tag{1}$$

This fitting allows us to also determine the phase velocity of the transverse waves, calculated to be 260 m s^{-1}. The velocity is $c = \sqrt{T/\sigma}$ so we can further derive the average stress (T) within the system, found to be

0.342 GPa, if we take the density of the MoS_2 (σ) as 5.06 g cm^{-3}. The discussion related with the plate or membrane behaviour is in Supplementary information figure S9.

Conclusion

We have developed a method for imaging the resonant modes of 2D NEMS. Performing RF spectra of the reflected intensity of a laser beam at each point of a scan area allows us to conduct a quick survey of the modes with frequency and spatial information.

Once the modal spectra are characterised, high resolution raster images can be obtained using lock-in techniques to get more precise magnitude and phase information of each of the resonant modes. To the best of our knowledge, this is the first time that resonant modes of 2D drum resonators have been faithfully imaged at low temperatures. Our results contribute with a new insight in the dynamical behaviour of electromechanical resonators based on two dimensional materials.

Our results show how nominally circular devices behave as elliptical membranes. Small deviations from circularity lead to a set of modes that correspond to those of elliptical drum resonators. Furthermore, we carried out our experiments at different temperatures, showing how the degeneracy of some modes breaks at lower temperatures when their spectral shapes narrow down.

Further research has to be carried out to clarify if this asymmetry is down to a tension field as a result of the exfoliation procedure, a systematic error in the lithography optics such as a small amount of astigmatism, or even to a preferential orientation of the crystal lattice of the membrane.

These results can help design new transduction schemes for drum resonators, since the frequency ratios of the modes and the physical position of the antinodes are different from those of circular membranes. In many cases, the laser is focused on the centre of the resonator, which is not ideal if the modes were to be elliptical, since many of the resonant modes will present a node there, minimising the optical contrast for the electro-optical conversion. Taking into account the mode shapes can help develop new optical transduction schemes for light amplitude or frequency modulation.

Membrane systems can transmit only in-plane forces and have no bending stiffness. Whereas plate systems have significant bending stiffness, loaded in out-of-plane direction. Comparing each systems (Supplementary information figure 9), let us conclude that our system has to be model as a membrane system, although it is 25 nm thick. This is opposed to the results in many articles [23, 31] in which they claim that the elastic transition begins for thickness above 7 nm.

Methods

Device fabrication

Onto a 290 nm-SiO_2/Si(N++) wafer, we deposit Ti(5 nm)/Au(40 nm) parallel electrodes with optical lithography and e-beam evaporator. We pattern circular and rectangular shapes with a radius of r $\approx$ 2.5 μm, and sides of L $\approx$ 5 μm and M $\approx$ 10 μm through a second optical lithography step. Following that, we selectively remove the SiO_2 on the uncovered areas with HF, creating similar wells on the whole device in one step and with a depth defined by the thickness of the SiO_2 layer (Supplementary figure 3). Different etching techniques were considered, such as focused ion beam milling and plasma etching (Supplementary figures 1 and 2), but we opted for the HF wet etching for its chemical sensitivity, for which we can use the lithographic resist or the gold contacts as hard masks. HF selectively removes the 290 nm of silicon oxide and will not etch silicon away. This technique yields wells of a constant and well-defined depth, with the minor drawback of producing a slight underetching below the gold contacts if the gold is used as the mask.

After the electrodes deposition and holes etching, MoS_2 flakes are deterministically transferred onto the wells using a well-known thermally assisted mechanical exfoliation [45], forming the desired capacitor structure that will act as a drum resonator. The thickness of the flakes ranges from 10 nm to 30 nm (Supplementary information figure 10).

A total of 40 samples have been fabricated comprising over 10 resonators each. Representative results from three of them are shown in this article. The results shown in the main text of this paper correspond to one device. The rest of them show similar qualitative behaviour, differing only in their characteristic frequencies due to thickness and width variations.

Preliminary characterisation

AFM characterization is used to estimate the thickness of the flake and relative positions. Which are 25 nm and around 280–290 nm from the bottom to the supported flake, respectively. This results are shown in Supplementary information figure S10 and Supplementary information figure S11. The cavity depth is

measured to know exactly the amount of etched SiO_x. With the AFM measurement of the suspended part, we can estimate the initial distance between the flake and the bottom of the well before applying any voltage.

Cryogenic microscopy setup

The devices are placed in a closed-cycle cryostat (Attocube AttoDRY 800) with a coarse XYZ piezoelectric micro positioner (1x Attocube ANPz102/RES/LT, 2x Attocube ANPx311/RES/LT) and a fine XYZ piezo scanner with nanometric resolution (1x Attocube ANSz100/LT, 1x Attocube ANSxy100/LT). We have optical access to the devices through optical windows and a microscope objective (Attocube LT-APO/VIS/0.82) situated inside the cryostat.

A CMOS camera (Thorlabs DCC1645C-HQ) can be placed in the optical path, allowing us to image the MoS_2 resonator and track the exact position of the laser spot over its surface. The Fabry–Perot cavity created by the MoS_2 and the bottom Si surface, transduce the vertical displacement of the membrane into changes of the reflected intensity of the laser.

The reflected signal at each point is registered using a 150 MHz bandwidth photodiode (Thorlabs PDA10A2). This signal is used for all the different techniques used throughout this paper: acquisition of the reflectivity reference images, reflectance spectra and high resolution imaging.

The illumination source used for probing the optical signal of the resonators is a Modu-Laser Stellar Pro Ar-ion laser (CW, 488 nm, up to 50 mW). For this work we kept the laser power below 1.5 mW, which keeps the power density reaching the device to under 200 mW cm^{-2} after crossing the different elements of the optical setup.

Electrical excitation of device resonance

Electrical signals are fed to the device via a high-vacuum RF feedthrough installed in the cryostat. We electrically drive the membrane by applying DC and AC voltage between the two separated electrodes, so the total voltage is $V = V_{DC} + \frac{V_{pp}}{2}$, using either the function generator of the digital signal processor (Moku:lab, up to $V_{pp} = 2$ V, $V_{DC} = 1$ V), or an external arbitrary function generator (RS Pro AFG-31051, up to V_{pp} up to 20 V) depending on the experiment requirements.

Frequency-resolved optical measurement of the mechanical modes

The optical signal reflected from the device is detected using a 150 MHz bandwidth amplified silicon photodiode (Thorlabs PDA10A2) and fed to a Moku:Lab signal processor. Using the API provided by Moku and the trigger ports of our Attocube scanner we wrote a Python script that enables us to measure the frequency response spectrum of the device at each point of a defined scan area. This enables us to perform fast spectral maps by scanning over the sample while recording with the frequency response with spatial resolution, which serve us as a quick survey method to identify the different resonant modes. Once this survey is finished, we can switch the Moku:lab to work as a lock-in amplifier and conduct higher resolution scans at specific frequencies, phases and amplitudes to characterise the individual modes.

Acknowledgment

The authors would like to acknowledge the financial support by the Spanish Ministry of Science, Innovation and Universities through the project MAINSTREAM PID2022-137779OB-C42, MAD4SPACE TEC-2024/TEC-182, DEFROST ONR N62909-19-1-2053, Severo Ochoa Centre of Excellence CEX2020-001039-S, and the FPI predoctoral fellowship PRE2022-103066 (J G-P).

Data availability statement

All data that support the findings of this study are included within the article (and any supplementary files).

Author contributions

Julia García-Pérez 0000-0002-4527-6145
Formal analysis (equal), Investigation (equal), Methodology (equal), Software (equal), Visualization (equal), Writing – original draft (equal), Writing – review & editing (equal)

Daniel Granados 0000-0001-7708-9080
Conceptualization (equal), Project administration (lead), Resources (lead), Supervision (lead), Writing – review & editing (equal)

Ramón Bernardo-Gavito 0000-0001-6881-2599
Conceptualization (equal), Formal analysis (equal), Investigation (equal), Methodology (equal), Software (equal), Supervision (equal), Visualization (equal), Writing – original draft (equal), Writing – review & editing (equal)

References

[1] Seshadri R 2025 Response of the quantum ground state to a parametric drive *Phys. Lett.* A **539** 130369
[2] Rufo P G C, Mazumdar A and Sabín C 2025 Genuine tripartite entanglement in graviton-matter interactions *Phys. Rev.* A **111** 22444
[3] Lee J, Sim J H, Ahn J K and Kwon Y W 2022 An open dataset for deep learning-based earthquake detection using MEMS sensors *Proc. - 2022 IEEE Int. Conf. on Big Data, Big Data (Institute of Electrical and Electronics Engineers Inc., 2022)* 6755–7
[4] Prasanna R *et al* 2022 Saving precious seconds'—a novel approach to implementing a low-cost earthquake early warning system with node-level detection and alert generation *Informatics* **9** 25
[5] Ann Mabrouk P 2005 Modern raman spectroscopya practical approach by ewen smith (Strathclyde University, Glasgow, U.K.) and geoffrey dent (Intertek ASG and UMIST, Manchester, U.K.) *J. Am. Chem. Soc.* (Wiley) 11876–7
[6] Bachtold A, Moser J and Dykman M I 2022 Mesoscopic physics of nanomechanical systems *Rev. Mod. Phys.* **94** 45005
[7] McRae A C *et al* 2024 Mechanical control of quantum transport in graphene *Adv. Mater.* **36** 1–9
[8] Luo Y, Liu N, Li X, Hone J C and Strauf S 2019 Single photon emission in WSe_2 up 160 K by quantum yield control *2D Mater.* **6** 050173
[9] Zhang X *et al* 2020 Dynamically-enhanced strain in atomically thin resonators *Nat. Commun.* **11** 1–9
[10] Duraffourg L and Arcamone J 2015 From MEMS to NEMS *Nanoelectromechanical Systems* (Wiley) 1–11
[11] Davidovikj D, Scheepers P H, Van Der Zant H S J and Steeneken P G 2017 Static capacitive pressure sensing using a single graphene drum *ACS Appl. Mater. Interfaces* **9** 43205–10
[12] Xu B *et al* 2022 Nanomechanical resonators: toward atomic scale *ACS Nano* **16** 15545–85
[13] Lemme M C *et al* 2020 Nanoelectromechanical sensors based on suspended 2D materials *Research* **2020**
[14] Lee C, Wei X, Kysar J W and Hone J 2008 Measurement of the elastic properties and intrinsic strengthof monolayer graphene *Science* **80** 385–8
[15] Aguila M A C *et al* 2022 Fabry–Perot interferometric calibration of van der Waals material-based nanomechanical resonators *Nanoscale Advances* **4** 502–509
[16] Zhang P, Jia Y, Liu Z and Yang R 2024 Strain-enhanced dynamic ranges in two-dimensional MoS_2 and $MoTe_2$ nanomechanical resonators *Appl. Phys. Rev.* **11** 011410
[17] Wang C, Ning L, Zhao W and Li F 2024 Quaternary piezoelectric ceramics with ultra-high mechanical quality factor *Mater. Res. Bull.* **180** 112995
[18] Morell N *et al* 2016 High quality factor mechanical resonators based on WSe_2 monolayers *Nano Lett.* **16** 5102–8
[19] Wan Z *et al* 2024 A review of acoustic devices based on suspended 2d materials and their composites *Adv. Funct. Mater.* **34** 1–39
[20] Warminski J, Kecik K, Mitura A and Bochenski M 2012 Nonlinear phenomena in mechanical system dynamics *J. Phys. Conf. Ser.* **382** 012004
[21] Keşkekler A *et al* 2021 Tuning nonlinear damping in graphene nanoresonators by parametric–direct internal resonance *Nat. Commun.* **12** 1099
[22] Lee J, Shaw S W and Feng P X L 2022 Giant parametric amplification and spectral narrowing in atomically thin MoS_2 nanomechanical resonators *Appl. Phys. Rev.* **9** 011404
[23] Castellanos-Gomez A *et al* 2013 Single-layer MoS_2 mechanical resonators *Adv. Mater.* **25** 6719–23
[24] Kim S, Yu J and Van Der Zande A M 2018 Nano-electromechanical drumhead resonators from two-dimensional material bimorphs *Nano Lett.* **18** 6686–95
[25] Steeneken P G, Dolleman R J, Davidovikj D, Alijani F and van der Zant H S J 2021 Dynamics of 2D material membranes *2D Mater.* **8** 42001
[26] Barton R A *et al* 2011 High, size-dependent quality factor in an array of graphene mechanical resonators *Nano Lett.* **11** 1232–6
[27] Wang Z *et al* 2016 Resolving and tuning mechanical anisotropy in black phosphorus via nanomechanical multimode resonance spectromicroscopy *Nano Lett.* **16** 5394–400
[28] Zheng X Q, Lee J and Feng P X L 2017 Hexagonal boron nitride nanomechanical resonators with spatially visualized motion *Microsystems Nanoeng* **3** 1–8
[29] Davidovikj D *et al* 2016 Visualizing the motion of graphene nanodrums *Nano Lett.* **16** 2768–73
[30] Liang Y *et al* 2025 Tunable anisotropy in wide-bandgap 2D crystal CaNb2O6 utilizing nanomechanical resonators *Int. J. Extrem. Manuf.* **7** 045505
[31] Lee J, Wang Z, He K, Shan J and Feng P X L 2013 High frequency MoS_2 nanomechanical resonators *ACS Nano* **7** 6086–91
[32] Davidovikj D *et al* 2017 Nonlinear dynamic characterization of two-dimensional materials *Nat. Commun.* **8** 1253
[33] Lee J *et al* 2018 Electrically tunable single- and few-layer MoS_2 nanoelectromechanical systems with broad dynamic range *Sci. Adv.* **4** 1–8
[34] Wang Z, Lee J, He K, Shan J and Feng P X L 2014 Embracing structural nonidealities and asymmetries in two-dimensional nanomechanical resonators *Sci. Rep.* **4** 1–7
[35] Zhu J *et al* 2023 Achieving 1.2 fm/Hz1/2 displacement sensitivity with laser interferometry in two-dimensional nanomechanical resonators: pathways towards quantum-noise-limited measurement at room temperature *Chinese Phys. Lett.* **40** 038102
[36] Sanz-Jiménez A *et al* 2022 High-throughput determination of dry mass of single bacterial cells by ultrathin membrane resonators *Commun. Biol.* **5** 1–10
[37] Sanz-Jiménez A *et al* 2023 Square membrane resonators supporting degenerate modes of vibration for high-throughput mass spectrometry of single bacterial cells *ACS Sens.* **8** 2060–7
[38] Santoso Tamsir A, Tannu Wijaya S and Yeop Majlis D B 2014 Adjustable resonance frequency of RF-MEMS capacitor by using comb-drive actuators: a design approaches *Makara J. Technol.* **18** 59
[39] Kafi F, Pilevar Shahri R, Benam M R and Akhtar A 2017 Tuning optical properties of MoS_2 bulk and monolayer under compressive and tensile strain: a first principles study *J. Electron. Mater.* **46** 6158–66

[40] Galaviz-Aguilar J A, Vargas-Rosales C, Falcone F and Aguilar-Avelar C 2025 Field-programmable gate array (FPGA)-based lock-in amplifier system with signal enhancement: a comprehensive review on the design for advanced measurement applications *Sensors* **25** 1–24
[41] Beccari A *et al* 2022 Strained crystalline nanomechanical resonators with quality factors above 10 billion *Nat. Phys.* **18** 436–41
[42] Waller M D 1950 Vibrations of free elliptical plates *Proc. Phys. Soc. Sect.* B **63** 451–5
[43] Buchanan G R and Peddieson J 2005 A finite element in elliptic coordinates with application to membrane vibration *Thin-Walled Struct.* **43** 1444–54
[44] Rossing T D and Fletcher N H 2004 Two-Dimensional Systems: Membranes and Plates *Principles of Vibration and Sound* ed T D Rossing and N H Fletcher (Springer) 65–94
[45] Mak K F, Lee C, Hone J, Shan J and Heinz T F 2010 Atomically thin MoS_2: a new direct-gap semiconductor *Phys. Rev. Lett.* **105** 2–5